Co Single Atoms in ZrO_2 with inherent oxygen vacancies for selective hydrogenation of CO_2 to CO

Nazmul Hasan MD Dostagir,[a,b] Rattanawalee Rattanawan,[a] Min Gao,[a] Jin Ota,[a,c] Jun-ya Hasegawa,[a] Kiyotaka Asakura,[a,c] Atsushi Fukouka,[a]* and Abhijit Shrotri[a]*

[a]*Institute for Catalysis, Hokkaido University, Kita 21 Nishi 10, Kita-ku, Sapporo, Hokkaido 001-0021, Japan,*

[b]*Graduate School of Chemical Sciences and Engineering, Hokkaido University, Kita 13 Nishi 8, Kita-ku, Sapporo, Hokkaido 060-8628, Japan*

[c]*Division of Quantum Science and Engineering, Graduate School of Engineering, Hokkaido University, Kita 21-Nishi 10, Kita-ku, Sapporo, Hokkaido 001-0021, Japan*

Abstract

Controlling the selectivity of products among CO, methane and methanol is a challenge in CO_2 hydrogenation. Catalysts with oxygen vacancies are helpful for CO_2 activation but they exhibit poor CO selectivity as intermediates stabilized over oxygen vacancies undergo deep hydrogenation to methanol and methane. Here, we report the synthesis of a catalyst with isolated Co atoms in ZrO_2 that exhibits oxygen vacant sites near Co atoms owing to charge imbalance between cations. The resulting catalytic site effectively adsorbs CO_2 and also achieves more than 95% CO selectivity during hydrogenation. The CO selectivity was independent of other reaction parameters such as reaction

pressure, space velocity and H_2/CO_2 ratio. *Operando* DRIFTS analysis showed that CO_2 was first hydrogenated to formate and it preferentially decomposed to CO under the reaction condition instead of forming methanol. Furthermore, the adsorption of CO on active sites was less favorable than the adsorption of CO_2, limiting its further hydrogenation to methane. The synergy between Co and Zr was crucial for generation of oxygen vacancy and stabilization of formate species as an intermediate for CO formation. This study shows the importance of strategic design of atomic interface to control selectivity of a specific product CO from CO_2 hydrogenation.

KEYWORD: CO_2 hydrogenation, cobalt catalyst, oxygen vacancy, in situ DRIFT, doped oxide, RWGS reaction, formate

Introduction

Reductive recycling of CO_2 is attractive as a means of producing renewable chemicals without utilizing fossil fuels. CO_2 recycling involves its hydrogenation to C1 compounds (CO, CH_3OH and CH_4) that are further converted to value added chemicals. Among the C1 products, CO is a resource for synthesis of alcohols, liquid hydrocarbons, and organic acids using the existing infrastructure for syngas conversion.[1–7] In hydrogenation of CO_2 to CO (Equation 1), also known as reverse water gas shift reaction (RWGS), increasing CO selectivity is a challenge because methanol and methane are formed simultaneously.

$$CO_2 + H_2 \leftrightarrow CO + H_2O \quad (1)$$

Significant efforts have been devoted towards designing catalysts for maximizing selectivity and understanding the underlying mechanism of CO formation.[8–10]

When supported metal catalysts are used for CO_2 hydrogenation, the metal particle size often dictates the functionality of the catalyst.[11–18] It is generally accepted that nanoparticles favor the formation of methane, whereas single atom catalysts favor CO formation.[19] Metal nanoparticles strongly adsorb CO and its hydrogenation by dissociatively adsorbed H species on the metal surface increases methane selectivity. Over single metal sites, weak adsorption of CO limits its further hydrogenation and improves CO selectivity.[15,20] However, the adsorption/desorption behavior of CO over single metal atoms is not the only factor and the interface of single metal atoms with oxide support plays a crucial role in stabilizing the reaction intermediates. For example, in a Ru/CeO_2 single atom catalyst, CO was stabilized at the interface and methane was produced by its successive hydrogenation.[21] Therefore, along with the isolation of metal atom sites it is important to understand the role of interfacial site to control the activity and selectivity of catalysts.[22–25]

Design of catalysts with interfacial sites containing oxygen vacancies has emerged as a promising strategy for preparing highly active catalyst for CO_2 hydrogenation.[25] The oxophilic nature of oxygen vacancy enhances adsorption of CO_2 and makes it susceptible to hydrogenation by adjacent metal atoms resulting in high activity.[26] The oxygen vacant sites promotes deep hydrogenation of CO_2 to CH_3OH and CH_4 as the vacancy tends to stabilize the reaction intermediates such as formate and methoxy species.[27–29] Isolation of Rh atoms over In_2O_3 catalyst with oxygen vacancy promoted hydrogen dissociation and increased methanol formation rate without influencing the selectivity.[30] Similarly, in a $ZnO\text{-}ZrO_2$ solid solution catalyst, methanol was formed via the hydrogenation of formate species stabilized at the interfacial site having oxygen vacancy.[29] Therefore, catalysts with isolated metal atoms adjacent to oxygen deficient interface tend to be more selective towards CH_3OH and CH_4 as the further hydrogenation of intermediates stabilized over the oxophilic interface is easier.

In contrast, here we show that high CO_2 hydrogenation activity with excellent CO selectivity can be achieved by isolated Co atoms dispersed in ZrO_2 through doping. We show that while formate is formed and stabilized over the oxophilic interface, it selectively decomposes to CO and H_2O instead of forming CH_3OH. The isolation of Co atoms restricted the formation of methane through adsorption and hydrogenation of CO over the metallic Co nanoparticles.

In our study, we synthesize Co doped ZrO_2 catalyst with 1 – 15 atom % loading to create isolate Co atoms with oxygen vacancies via charge imbalance of cations and apply this catalyst for CO_2 hydrogenation reaction. The structure of catalyst was clarified using various characterization methods. The catalytic activity was measured under varying reaction conditions and was correlated with catalytic property. *Operando* diffuse reflectance infrared Fourier transform spectroscopy (DRIFTS) analysis was used to identify reaction intermediates and clarify the mechanism. Insight into the effect of Co doping on oxygen vacancy formation and its effect on CO_2 activation was also elucidated using density functional theory (DFT) calculation. The nature and property of active sites are discussed in context of change in selectivity from methanol to CO to methane. This study achieves exceptional CO selectivity under versatile reaction conditions and addresses the crucial problem of selectivity control among CO_2 hydrogenation products while accounting for the mechanism of CO formation.

Results and Discussion

Preparation and characterization of doped and impregnated Co catalysts on ZrO_2

Co doped ZrO_2 catalysts were prepared by co-precipitation method and denoted as $CoZrO_x$ (Y), where Y is the atom % of Co with respect to total metal content (Y = (Co/Co + Zr) × 100). Co loading of 1-50 atom % was used for doped catalysts. For comparison, an impregnated catalyst was also

prepared (Co_3O_4/ZrO_2) with Co loading of 10 atom %. The measured bulk Co concentration in the doped catalysts was slightly lower than the theoretical values whereas the surface Co concentration was comparable to theoretical values (Figure S1). N_2 adsorption isotherms of all catalysts were similar and Co loading did not change the physical morphology of catalysts (Figure S2). In the X-ray diffraction (XRD) spectrum, undoped ZrO_2 exhibited both monoclinic and tetragonal features (Figure 1a). Doping of Co stabilized the tetragonal phase of ZrO_2 (*t*-ZrO_2), and phase pure tetragonal structure was obtained with cobalt loading of 5 atom% and higher. The transformation of monoclinic phase to tetragonal phase in doped catalysts was due to incorporation of Co in the ZrO_2 crystal. Formation of CoO or Co_3O_4 was not evident except when Co loading was 50 atom% and for impregnated Co_3O_4/ZrO_2. For these two catalysts diffraction peaks for Co_3O_4 were observed. In stable Co doped ZrO_2 catalysts, the (101) reflection of *t*-ZrO_2 shifted to higher 2θ value with increasing Co loading (Figure 1b). The shift was caused by reduction in interplanar spacing in ZrO_2 owing to the smaller ionic radius of Co^{2+} (0.74 Å) in comparison to Zr^{4+} (0.84 Å).[31] This was also corroborated with the gradual decrease in lattice parameters with increasing Co doping amount (Figure S3). The change of ZrO_2 phase from monoclinic to tetragonal upon Co incorporation and the gradual reduction in interplanar spacing and lattice parameter of ZrO_2 with increasing Co loading shows homogeneous doping of Co in ZrO_2. The phase transition in ZrO_2 with Co loading was also evident in the Fourier transform of extended X-ray absorption fine structure (EXAFS) analysis of Zr k edge for doped catalyst (Figure S4). Undoped ZrO_2 and $CoZrO_x$ (1) exhibited a monoclinic structure with Zr-O and Zr-Zr distances of 2.12 and 2.45 Å respectively. Tetragonal ZrO_2 was observed for $CoZrO_x$ (5), $CoZrO_x$ (10), $CoZrO_x$ (15) catalysts as the Zr-O distance reduced to 2.08 Å and the Zr-Zr distance

increased to 3.65 Å. $CoZrO_x$ (50) was amorphous in XRD but showed features of monoclinic ZrO_2 lacking long range order in EXAFS.

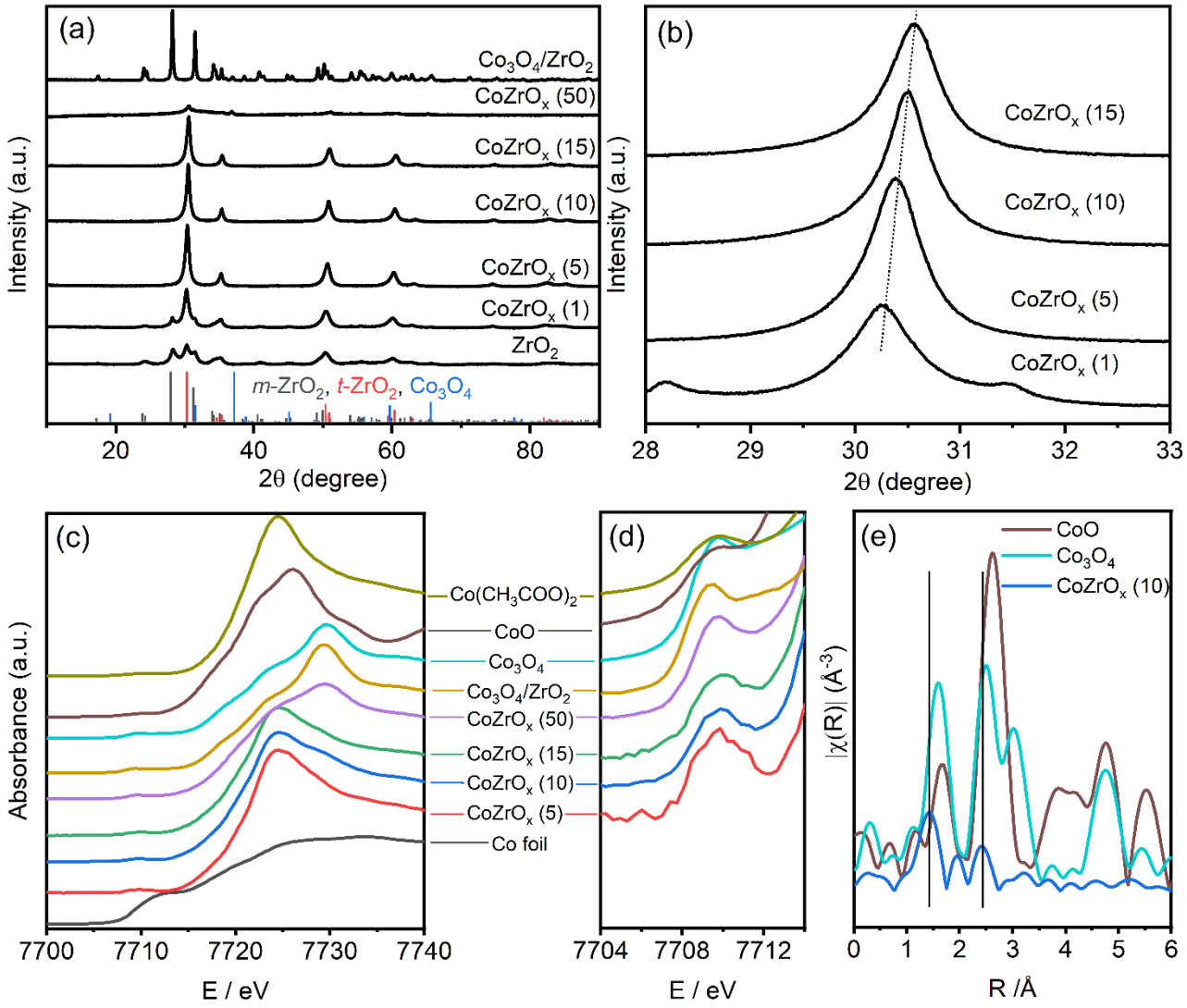

Figure 1: (a) XRD patterns of $CoZrO_x$ (Y) and Co_3O_4/ZrO_2 catalysts. *m*-ZrO_2 = monoclinic ZrO_2 (JCPDS card no. = 01-078-1807), *t*-ZrO_2 = tetragonal ZrO_2 (JCPDS card no = 01-080-0965) and Co_3O_4 (JCPDS card no = 00-043-1003). (b) Shifting of (101) plane of *t*-ZrO_2 as a result of doping of Co. (c) XANES spectrum of doped and impregnated catalysts along with standard Co compounds.

(d) Expanded spectra showing the pre-edge region for Co XANES spectrum. (e) Fourier transform of EXAFS region for $CoZrO_x$ (10) catalyst and reference Co oxides.

The Co K-edge X-ray absorption near edge spectrum (XANES) spectra for all catalysts along with reference materials is shown in Figure 1c. The edge position for stable doped catalysts (X = 5, 10 and 15) was at 7722 eV, which was assigned to divalent Co^{2+} species as the valence state is relative to edge position for Co (Figure S5). $CoZrO_x$ (50) was the exception among doped catalysts and had a higher edge position of 7726 eV due to the presence of Co^{3+} as found in Co_3O_4. In the pre-edge region (Figure 1d), the height of pre-edge peak around 7710 eV was assigned to 1s to 3d transition, which was smaller when centrosymmetry was present, for example in CoO and $Co(CH_3COO)_2$. Larger peaks were observed for Co_3O_4/ZrO_2 and $CoZrO_x$ (50), containing Co_3O_4 having a tetrahedral structure without centrosymmetry. The pre-edge peaks for doped catalysts were larger than CoO and $Co(CH_3COO)_2$ indicating a loss of centrosymmetry in the Co^{2+} local structure owing to its doping in the tetragonal ZrO_2. The EXAFS region for $CoZrO_x$ (10) catalyst is shown in Figure 1e. The noise in EXAFS region was high due to the large background absorbance of ZrO_2. Nevertheless, the Fourier transform of $CoZrO_x$ (10) differed from that of CoO and Co_3O_4. Curve fitting showed that the Co-O distance of 1.88 Å in $CoZrO_x$ (10) was shorter than that of CoO (Table S1). The small peak appearing at 2-3 Å was well fitted with Co-Zr interaction although with a short bond distance of 2.71 Å (Figure S6). Further studies are necessary to confirm the presence of Co-Zr interaction at this distance. We could conclude that the Co atoms were divalent in the doped catalysts and did not resemble the crystal structure of CoO or Co_3O_4.

Nature of Co atoms in $CoZrO_x$ (10) catalyst was investigated in detail and compared with impregnated Co_3O_4/ZrO_2. Figure 2 shows the high angle annular dark field scanning transmission electron microscopy (HAADF-STEM) images of catalysts. Co particles or clusters were not observed in the doped catalyst (Figure 2a). Although atomic resolution was obtained, identification of individual Co atoms was not possible from STEM image because the Co and Zr atoms appeared with the same brightness owing to their similar atomic numbers. We performed high resolution electron energy loss spectroscopy (EELS) to detect Co atoms in the lattice. Figure S7 shows the range of an EELS line scan following the metal atoms in lattice. The peaks for $L_{2,3}$ edge of Co were observed in the low-loss spectrum the region marked in red. Adjacent regions did not show presence of Co confirming the isolation of Co atoms in ZrO_2 matrix. In EDS mapping Co and Zr were distributed uniformly in the doped catalyst confirming homogeneous dispersion of Co (Figure 2b,c). In comparison, nanoparticles of Co_3O_4 supported over monoclinic ZrO_2 were observed for impregnated Co_3O_4/ZrO_2 catalyst (Figure 2d). EDS mapping showed that Co atoms were mainly confined to Co_3O_4 particles for impregnated catalysts (Figure 2e,f).

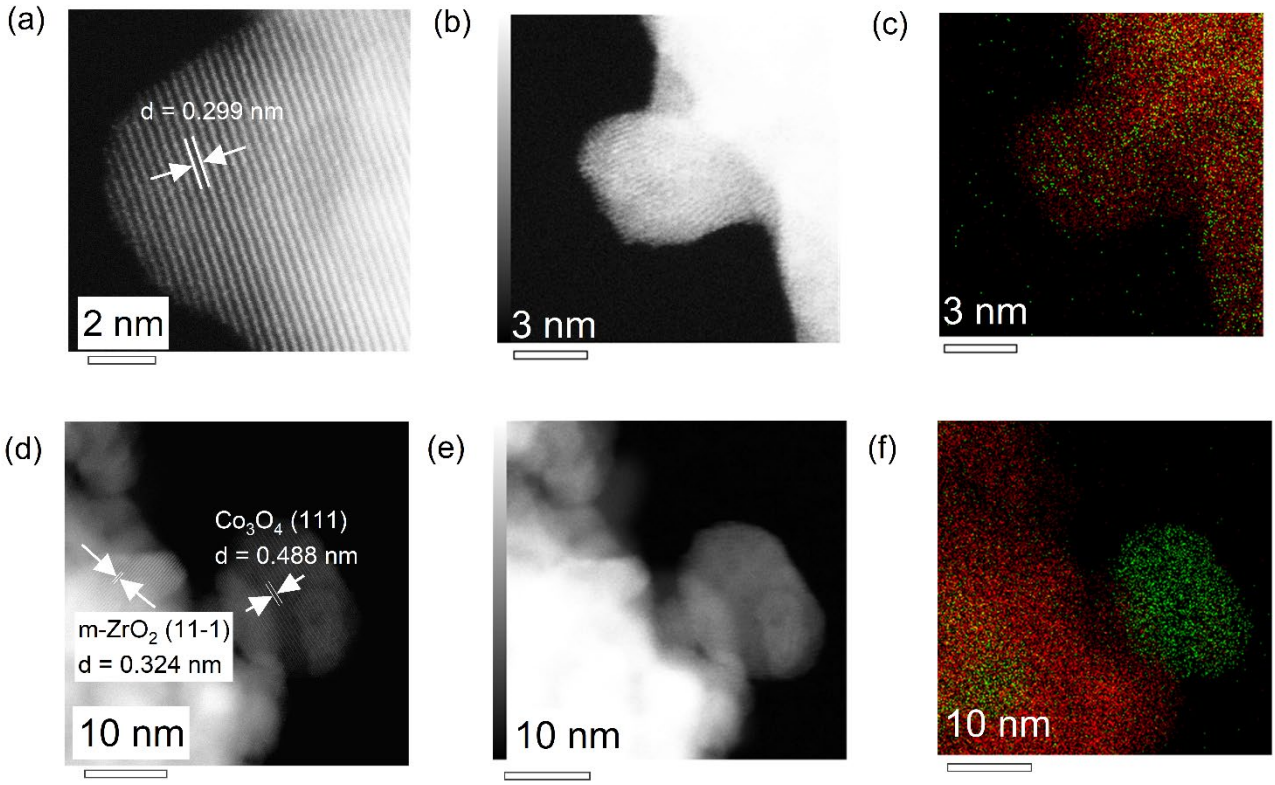

Figure 2: HAADF-STEM analysis of (a) $CoZrO_x$ (10) and (d) Co_3O_4/ZrO_2. EDX mapping of Co and Zr in $CoZrO_x$ (10) (b,c) and (e,f) 10% Co_3O_4/ZrO_2. Red and green colors in EDX mapping signify Zr and Co, respectively.

In the H_2 temperature programmed reduction (TPR) spectra, the impregnated Co_3O_4/ZrO_2 catalyst showed two peaks at 360 and 540 °C owing to the reduction of Co^{3+} to Co^{2+} and Co^{2+} to Co^0 species, respectively (Figure 3a). These two features are characteristics for reduction of Co_3O_4 particles. Pure ZrO_2 did not show any H_2 consumption because of its irreducible nature. $CoZrO_x$ (10) catalyst did not show prominent H_2 consumption peaks until 600 °C. Reduction features above 600 °C are indicative of highly dispersed Co species having strong interaction with the support.[32–34]

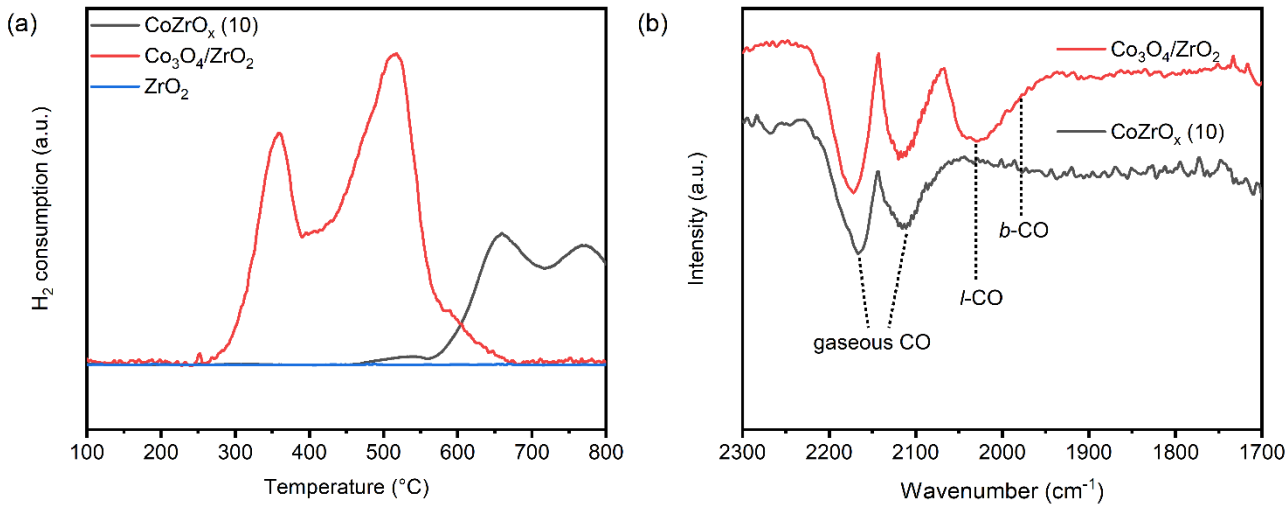

Figure 3: (a) H_2 TPR spectra of different catalysts. (b) CO DRIFTS over $CoZrO_x$ (10) (black line) and Co_3O_4/ZrO_2 (red line) showing gaseous CO and adsorbed CO in linear and bridge fashion (*l*-CO and *b*-CO respectively).

Further insight was obtained by observing CO adsorption at room temperature using DRIFTS analysis after subjecting the catalysts to reducing treatment at 450 °C (Figure 3b). Broad bands around 2174 and 2116 cm^{-1}, observed for both $CoZrO_x$ (10) and Co_3O_4/ZrO_2, were assigned to gaseous CO.[35] Peaks at 2030 and 1973 cm^{-1} (shoulder) appeared for Co_3O_4/ZrO_2, which are characteristics of the adsorption of CO in linear and bridging fashions over metallic Co particles.[35–38] These peaks for adsorbed CO species were absent for $CoZrO_x$ (10) catalyst. Oxygen bonded isolated Co atoms are known to have poor adsorption of CO, confirming the atomic dispersion of Co atoms in ZrO_2.[39]

The chemical environment around isolated Co atoms was investigated by X-ray photoelectron spectroscopy (XPS). In the Co 2p region 2p 3/2 peak at 781.0 eV and corresponding satellite peak at 786.0 eV were observed for Co^{2+} (Figure 4a).[40,41] Zr maintained its tetravalent Zr^{4+} oxidation state after Co doping (Figure 4b). The mismatch in oxidation states of Co^{2+} and tetragonal Zr^{4+} is expected

to create a charge imbalance in the crystal structure. Such imbalance can be mitigated by formation of oxygen vacancy close to Co atoms.[42] In the electron paramagnetic resonance (EPR) spectra (Figure 4c), sharp signals were present near 3500 G for pure ZrO_2, which were assigned to the presence of isolated oxygen vacancies and Zr^{3+}.[43] For $CoZrO_x$ (10) catalyst, the sharp signals were substituted with a broad signal appeared around 2900 G having a g factor of 2.26. With the increase in concentration of oxygen vacancies the paramagnetic centers tend to interact with each other and produces ferromagnetic feature. As a result, a broad signal appears in EPR spectrum at lower magnetic field with abundance of oxygen vacancies.[43,44] In the O1s region of the XPS spectrum a gradual increase in the peak centered at 532 eV was observed with increase in Co loading (Figure 4d). This peak ($O_{defects}$) was assigned to oxygen atoms near vacant sites and oxygen atoms present as -OH species on the surface. Formation of oxygen vacancies can facilitate the chemisorption of CO_2 on the catalyst surface.[45,46] Figure 4e shows the spectra for temperature programmed desorption of CO_2 (CO_2 TPD) for doped catalysts. The low temperature regions (100-300 °C) were assigned to physisorbed CO_2 and weakly adsorbed species. The desorption peak at 320 °C was assigned to chemisorbed CO_2, which increased in intensity with Co loading in accordance with generation of oxygen vacancy. A linear correlation was observed for increase in relative oxygen vacancy and chemisorbed CO_2 amount with increase in Co loading (Figure 4f). Consequently, we conclude that doping of ZrO_2 with Co led to formation of oxygen vacancy near isolated Co atoms because of charge imbalance in the crystal structure. These oxygen vacancies resulted in improved chemisorption of CO_2 as observed in CO_2 TPD spectra.

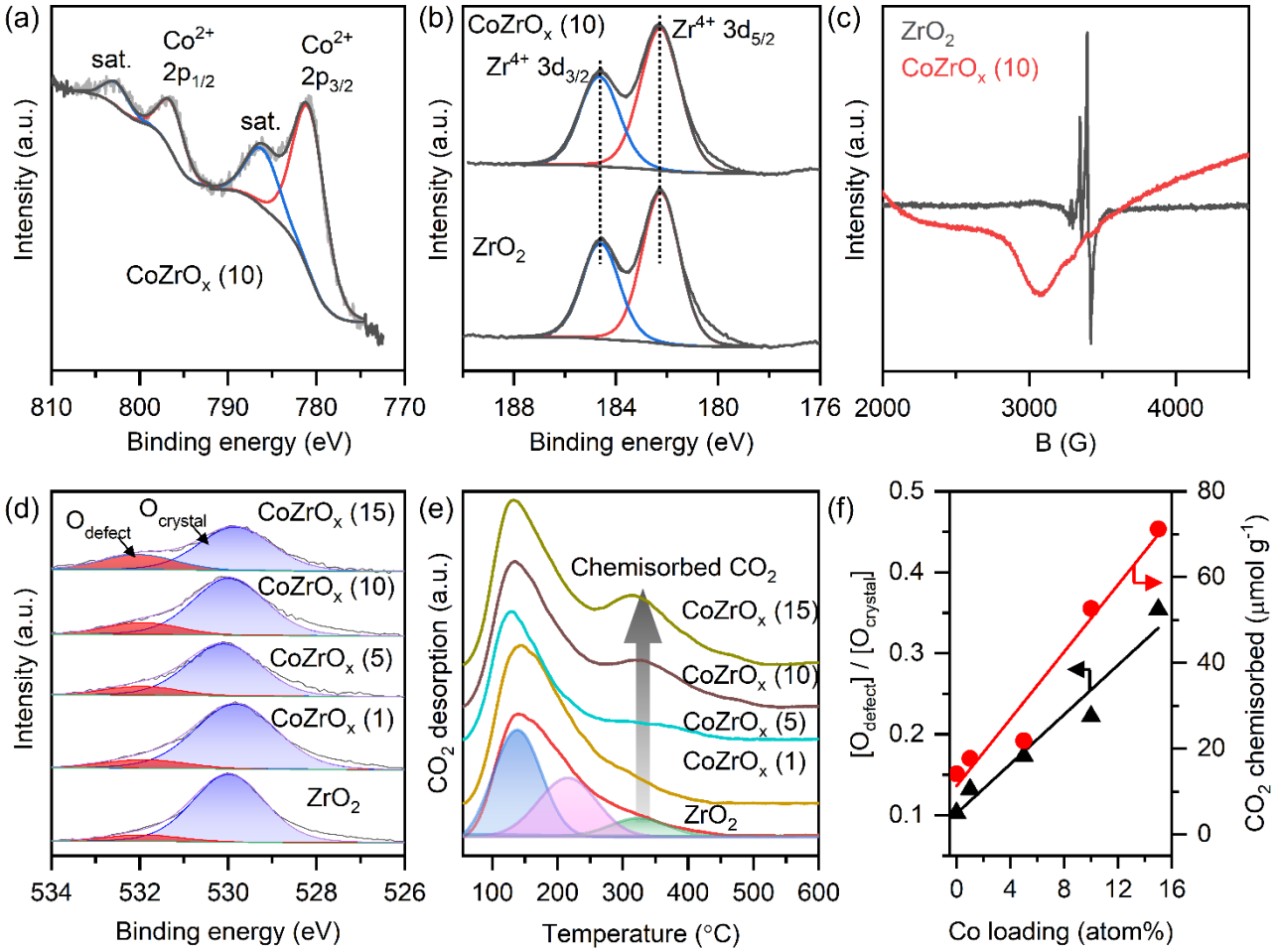

Figure 4: (a) Co 2p XPS spectra for $CoZrO_x$ (10) showing divalent nature of Co atoms after doping. (b) Zr 3d XPS spectra of $CoZrO_x$ (10) and ZrO_2. (c) EPR spectra of $CoZrO_x$ (10) and ZrO_2. (d) O1s XPS spectra for doped $CoZrO_x$ (Y) catalysts along with ZrO_2. (e) CO_2 TPD spectra showing increase in chemisorbed CO_2 amount at higher Co loading. (f) Correlation of theoretical Co loading with ratio of peaks in O1s XPS spectrum $[O_{defect}]/[O_{crystal}]$ and chemisorbed CO_2 amount, respectively.

Modeling the Co doped ZrO_2 surface and its interaction with CO_2

DFT calculations were carried out to understand the influence of Co doping on oxygen vacancy generation in ZrO_2, along with effect of Co and oxygen vacancy on CO_2 adsorption. The 101 facet

(ZrO_2 (101)) of *t*-ZrO_2 was chosen as the computational model because *t*-ZrO_2 was the only phase observed in XRD and the 101 facet of *t*-ZrO_2 is experimentally[47] and theoretically[48] reported to be the most stable one. The computational model of the Co doped ZrO_2 catalyst (Co-ZrO_2) was created by replacing one Zr atom at the top layer of the ZrO_2(101) by one Co atom**.**

The effect of Co doping was clarified by comparing the optimized geometries of ZrO_2 and Co-ZrO_2 surfaces. As shown in Figure 5, the geometry of ZrO_2 was slightly distorted with the doped Co atom. The Zr atom at the surface coordinated with 7 oxygen atoms in perfect ZrO_2 (101), where the threshold for M−O (M = Co or Zr) bond was set to 2.5 Å. In Co-ZrO_2, the Co atom coordinated with 5 O atoms. The imbalance in coordination number of Co and Zr atoms is likely to induce a vacancy site on the surface. Two possible vacancy sites were considered by removing oxygen atoms at *vo1* site of the top surface and *vo2* site of the subsurface as shown in Figure 5. The formation of oxygen vacancy was endothermic on pure ZrO_2 and exothermic after Co doping. The calculated formation energies of oxygen vacancy were 3.20 eV at the top layer and 2.70 eV at subsurface of ZrO_2. The formation energy decreased to -1.17 eV and -1.45 eV for Co-ZrO_2_vo1 and Co-ZrO_2_vo2, respectively. Therefore, in agreement with the experimental results, doped Co atom strongly promoted the formation of oxygen vacancy. Also, the Co atom moved inward and interacted with subsurface oxygen species generating a cavity around Co atom, which can act as active space for the hydrogenation reaction.

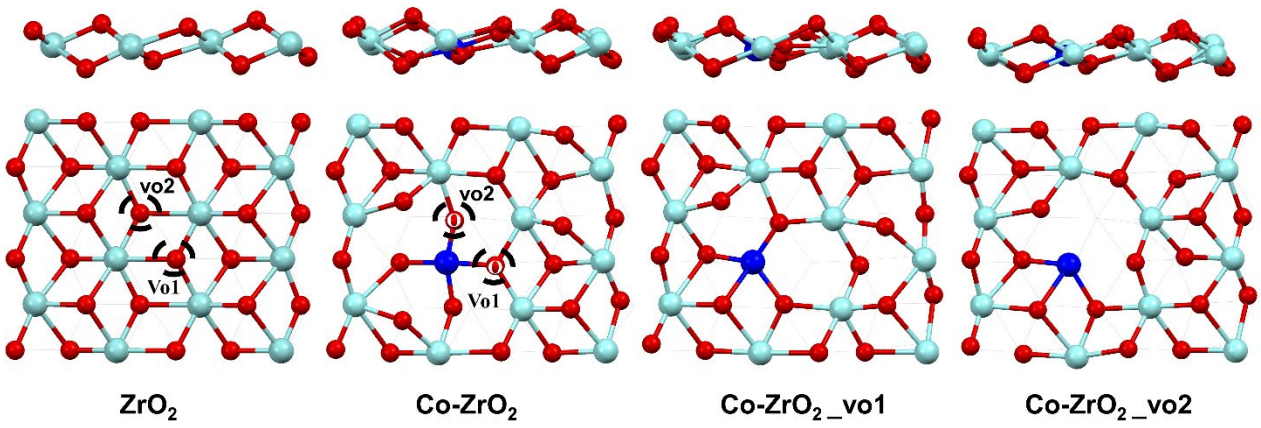

Figure 5: The side and top views for optimized ZrO_2 and Co-ZrO_2 surfaces with and without oxygen vacancies (denoted as Co-ZrO_2_v*x*, where *x* = o1, o2). The atoms at top layer and the second layer were represented by ball and stick, respectively. The other atoms were omitted for clarity. The dashed circle represents the position of oxygen vacancy. The Zr, O and Co atoms were represented in cyan, red and blue colors, respectively.

We also elucidated the influence of Co doping and the presence of oxygen vacancy on CO_2 adsorption. The adsorption of CO_2 molecule on metal oxide surfaces has been investigated extensively and various types of adsorption modes and sites have been reported.[49] We screened four possible modes at various sites for CO_2 adsorption as shown in Figure S8. The formation of Co-ZrO_2_vo1 and Co-ZrO_2_vo2 type vacancies would competitively exist in experimental system as they had similar energy of formation. Therefore, both geometries were considered for CO_2 adsorption. The optimized geometries of CO_2 adsorption can be divided into two groups, linear adsorption and the formation of carbonate species. The most stable geometry for linear CO_2 adsorption and carbonate species are shown in Figure 6a and 6b, respectively. CO_2 molecule can adsorb linearly on ZrO_2

surfaces with weak interaction between O atom of CO_2 and metal atom on the surface. No obvious changes were found after introducing Co atom and oxygen vacancy. Physical adsorption is usually a barrierless process, so the exothermic adsorption of linear CO_2 molecule occurs easily.

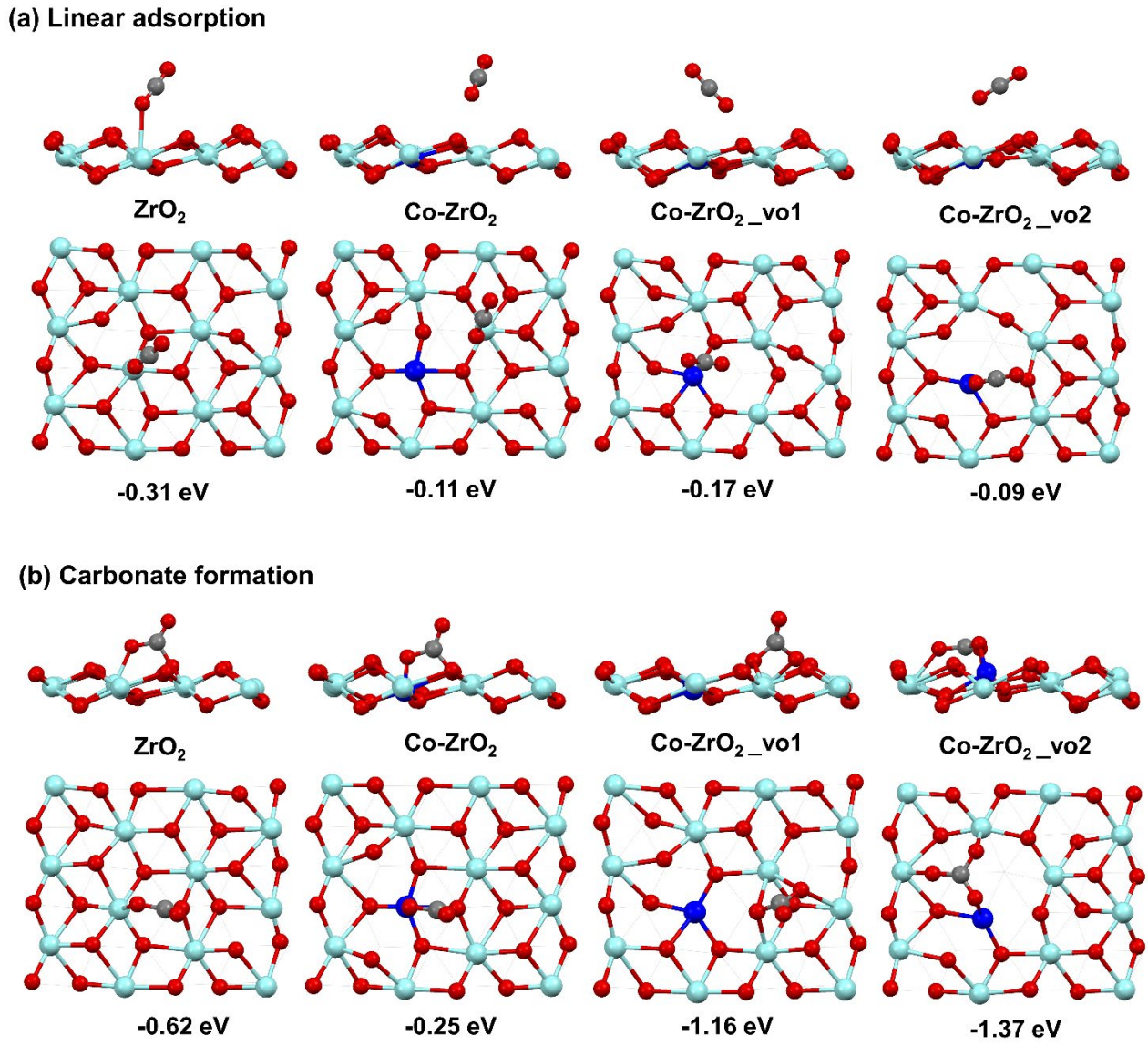

Figure 6: The most stable geometry for (a) linearly adsorbed CO_2 molecule and (b) formation of carbonate species on ZrO_2 and the surrounding of Co atom in Co-ZrO_2, Co-ZrO_2_vo1, and Co-

ZrO_2_vo2. The atoms at top layer and the second layer were represented by ball and stick, respectively. The other atoms were omitted for clarity. The corresponding adsorption energies for CO_2 molecule is shown at the bottom of each geometry. The Zr, O, Co and C atoms were represented in cyan, red, blue and gray colors, respectively.

The CO_2 adsorption in carbonate mode on ZrO_2 surface was more stable than the linear mode, with an adsorption energy of -0.62 eV. While the stability of carbonate species did not change with Co doping alone, the formation of oxygen vacancy promoted carbonate formation. The adsorption energies increase to ~1.2 eV in the presence of oxygen vacancies. The C atom of adsorbed CO_2 was bound to a lattice oxygen on the surface and the O atom of CO_2 interacted with both the unsaturated metal atoms and the oxygen vacant site. These results are consistent with experimental observation showing increased CO_2 chemisorption at the vacant site.

Catalytic activity for CO_2 hydrogenation

CO_2 hydrogenation ability of all catalysts was evaluated in a stainless-steel fixed bed reactor (Figure S9). In the presence of undoped ZrO_2, the CO_2 conversion was only 1.8% with 100% CO selectivity at 340 °C and 3 MPa (Figure 7a). For the Co-doped catalysts, CO_2 conversion increased with Co loading without significant change in CO selectivity. Highest CO space time yield (STY) of 3.8 μmol g^{-1} s^{-1} was obtained for $CoZrO_x$ (10) catalyst with 19% conversion and 97% CO selectivity and the rest being methanol. Methane was the predominant product in the presence of $CoZrO_x$ (50) and Co_3O_4/ZrO_2 catalysts, both of which contained Co_3O_4 particles. Therefore, all catalysts with single Co atoms in Zr network strongly favored CO formation over methane and methanol.

Reaction temperature influenced the product selectivity and methanol formation was higher at lower temperatures (Figure 7b). At 280 °C, $CoZrO_x$ (10) catalyst showed a CO_2 conversion of 1.5% with 29% methanol selectivity and 71% CO selectivity. This is expected as methanol formation is an exothermic reaction and is favored at lower temperatures. CO formation was prominent in the temperature range of 300-360 °C. Methane was detected at 380 °C and CO selectivity dropped to 84% at 420 °C with 16% methane. Dispersed Co atoms in ZrO_2 crystal were selective towards formation of methanol and CO at lower temperatures, and higher temperature caused further hydrogenation to methane. There was no drastic change in CO_2 conversion with temperature, suggesting that the catalyst structure was not altered even at high temperature.

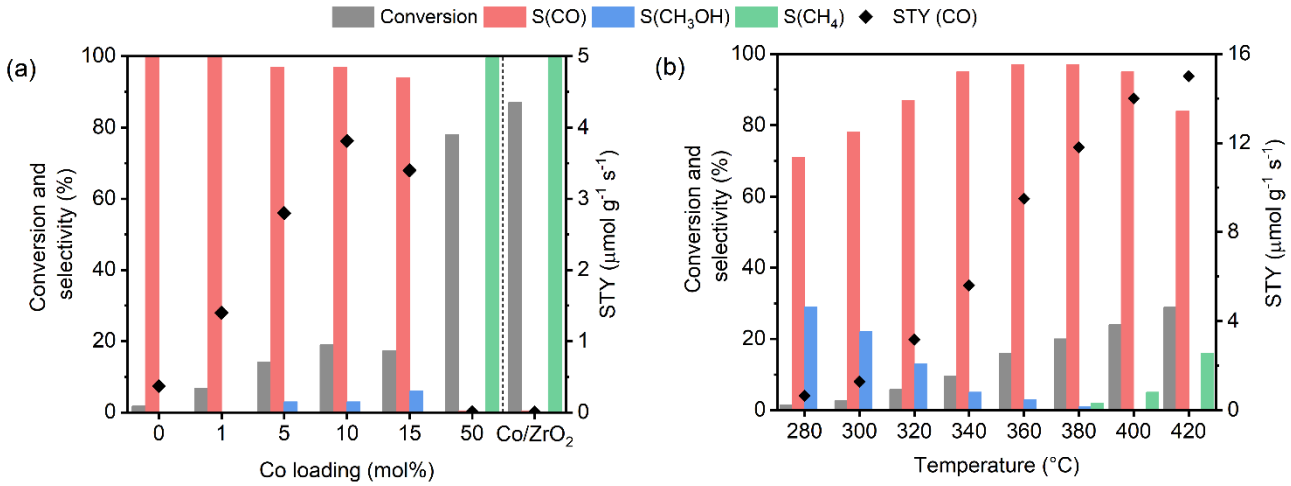

Figure 7: (a) Effect of Co loading on catalytic activity of doped ($CoZrO_x$ (Y)) and impregnated catalysts. Reaction condition: 340 °C, 10,000 mL h^{-1} g^{-1}, 3 MPa, H_2:CO_2 = 4:1 (b) Effect of temperature on the activity and product selectivity for $CoZrO_x$ (10) catalyst. Reaction condition: 30,000 mL h^{-1} g^{-1}, 3 MPa, H_2:CO_2 = 4:1.

CO selectivity was not influenced by change in any other reaction parameter. At ambient pressure, 9.8% CO_2 conversion was obtained with 100% CO selectivity over $CoZrO_x$ (10) (Figure S10a). Increasing the pressure to 4 MPa increased conversion to 21% with 96% CO selectivity. High CO selectivity regardless of pressure is unique because higher pressure promotes methanol and methane formation over conventional catalysts.[50,51] Decreasing the space velocity from 30,000 to 10,000 mL h^{-1} g^{-1} at 340 °C increased the conversion from 9.5% to 19% (Figure S10b). CO selectivity was above 95% in the tested space velocity (SV) range of 5,000-60,000 mL h^{-1} g^{-1} achieving a STY of 8.6 μmol g^{-1} s^{-1} at 60,000 mL h^{-1} g^{-1}. Altering the H_2 to CO_2 ratio also had negligible effect on CO selectivity and a constant STY was obtained at all ratios (Figure S10c). The activity of $CoZrO_x$ (10) is better than the non-noble metal catalysts in literature and is comparable to noble metal based catalysts (Table S2). In addition, high performance of Co doped ZrO_2 under versatile conditions is attractive because it allows optimization to suit downstream reactions.

The stability of the catalyst was evaluated under optimal condition of 340 °C, 3 MPa, 10,000 mL h^{-1} g^{-1} and H_2:CO_2 = 1:1 (Figure S11a). The catalytic activity slightly decreased in the first 70 h and then became stable. A STY of 3.5 μmol g^{-1} s^{-1} was stable over the course of 400 h time on stream. Used catalyst had a similar XRD profile as that of fresh $CoZrO_x$ (10) with a slight reduction in crystallize size from 16 nm to 12 nm (Figure S11b). In XPS spectra of used catalyst Co and Zr was present as divalent and tetravalent species and metallic Co was not detected (Figure S11c and d). This is corroborated with the H_2 TPR analysis of $CoZrO_x$ (10), which showed that Co species were not reduced at temperatures used for CO_2 hydrogenation (Figure 3a). The relative percentage of oxygen vacancy increased from 18% to 35% in the used catalyst (Figure S11e). Therefore, the catalyst was highly stable under the reducing conditions used during reaction.

Elucidation of mechanism and active site in doped catalyst

To understand the reaction mechanism, we employed operando DRIFTS to observe evolution of reaction intermediates along with CO formation. $CoZrO_x$ (10) was pretreated under He at 280 °C for 30 minutes in the IR cell (Operando DRIFTS set up shown in Figure S12). After pretreatment, reactant gases (H_2:CO_2 = 4:1) were fed at 280 °C followed by stepwise increase in temperature. For $CoZrO_x$ (10) catalyst, at 280 °C, several species were detected in the DRIFTS spectra (Figure 8a). Detailed assignment of peak is shown in Table S3. Peaks at 2972, 2882, 2740, 1585, 1384 and 1365 cm^{-1} were assigned as bidentate formate species ($HCOO^*$).[29,52–54] Peaks at 1632, 1221 cm^{-1} were assigned to bicarbonate species (HCO_3^*) and peaks around 1518, 1458, and 1423 cm^{-1} were assigned to carbonate species (CO_3^*).[54–56] Bicarbonate disappeared when temperature was increased to 300 °C along with reduction in carbonate species. In contrast formate formation was enhanced at higher temperature. At 340 °C, formate was the dominant species in the spectrum. Gaseous CO formation increased above 300 °C. CO formation was simultaneously measured by GC during IR measurement (Figure 8b). CO formation rate increased steadily with evolution of formate and was maximum at 340 °C. Therefore, the formation of CO over $CoZrO_x$ (10) catalyst seems to follow the formate pathway, which is also an intermediate for methanol formation.[57]

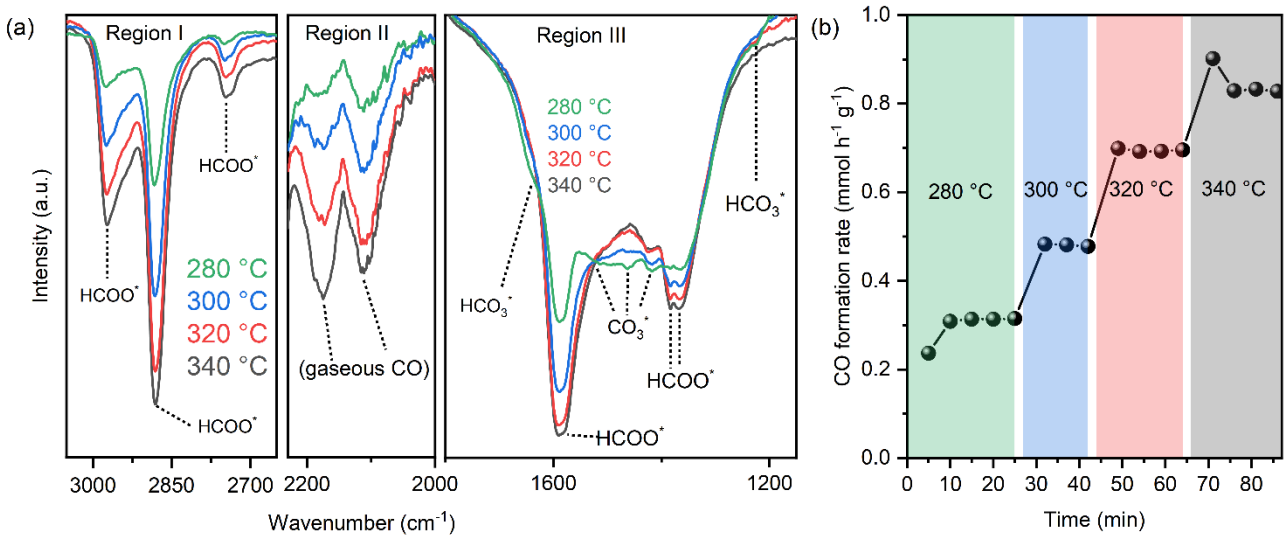

Figure 8: Operando DRIFTS experiment over $CoZrO_x$ (10) catalyst. (a) IR spectrum recorded at different temperature. Three regions were shown where "Region I" shows the spectrum in the range of 3050-2650 cm^{-1} (showing formate species), "Region II" shows the range 2230-2000 cm^{-1} (showing gaseous CO) and "Region III" shows the range 1700-1100 cm^{-1} (showing formate, bicarbonate and carbonate species). The y-axis scale is different for each region for clarity. (b) Formation rate of CO in the DFTIFS IR experiment. Reaction condition: 0.1 MPa, 280 – 340 °C, H_2:CO_2 = 4:1.

To clarify the formation of CO from formate over the surface of $CoZrO_x$ (10), we did the following experiment. First, CO_2 and H_2 were flown through the DRIFTS cell containing the $CoZrO_x$ (10) catalyst at 340 °C for 30 min. Then the gas flow was changed to He and the temperature was reduced rapidly to allow the intermediate species to remain on the catalyst surface. After cooling, the temperature was increased again in steps under the flow of H_2 and IR data was collected (Figure 9). With increasing temperature, adsorbed species such as carbonates and bicarbonate reduced (Figure 9a). The intensity of formate peak was stable until 300 °C and then reduced rapidly. In a separate experiment performed under the same conditions in the TPD instrument, we confirmed that evolution

of CO gas begins after 300 °C (Figure S13). Methoxy species appeared in the temperature range of 100–300 °C in accordance with methanol formation at lower temperature (Figure 9b). Appearance of methoxy under 300 °C and rapid decomposition of formate species after 300 °C along with CO formation is in line with the selectivity profile of products with temperature in Figure 7b. These experiments prove that formate is the intermediate for formation of CO and methanol over Co doped ZrO_2 catalyst.

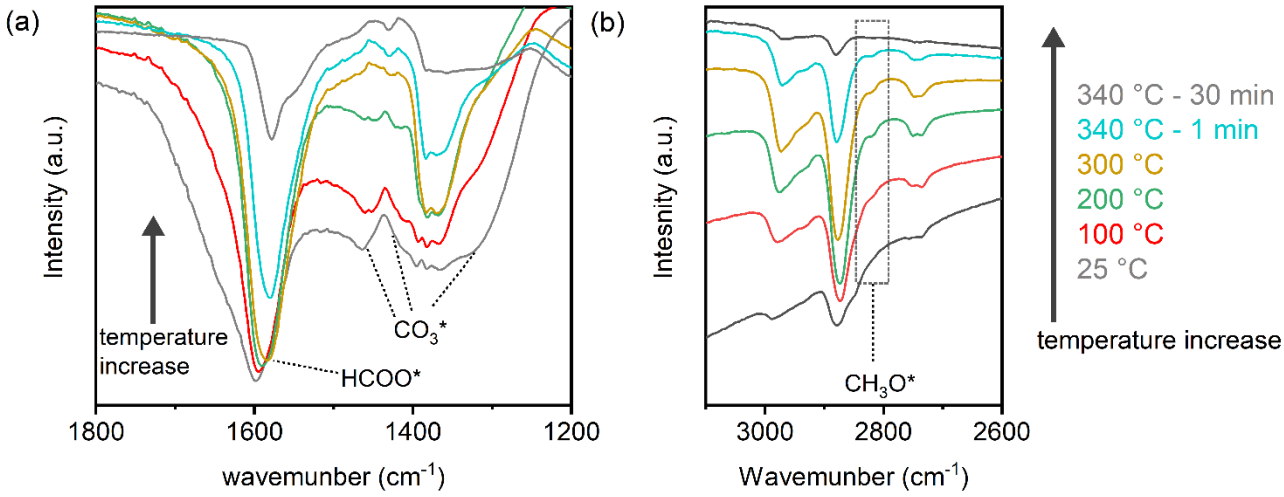

Figure 9: Evolution of different species (formed *in situ*) with temperature over $CoZrO_x$ (10). (a) Evolution of formate along with carbonate and bicarbonate species and (b) evolution of methoxy species (shown in dotted box).

In order to confirm if formate is formed by hydrogenation of adsorbed carbonate/bicarbonate species, we did the following two experiments using in situ DRIFTS instrument. In one experiment, the $CoZrO_x$ (10) catalyst was treated under H_2 atmosphere followed by purging gaseous H_2 with He and then flowing CO_2 while measuring DRIFT spectra. Formate formation was not evident and only carbonate and bicarbonate were detected during CO_2 flow (Figure S14a). In second experiment, we

treated the catalyst in opposite order, first with CO_2 followed by He and H_2. Mainly carbonate species were detected as a result of initial CO_2 adsorption. When H_2 flow started, carbonate was consumed and formate species along with gaseous CO (Figure S14b). These two experiments show that activation of CO_2 as carbonate is the most likely initial step and formate is formed afterwards via hydrogenation of carbonate species.

To gain insight into the nature of active site responsible for formate decomposition to CO we compared the *in-situ* DRIFTS spectra for $CoZrO_x$ (10) catalyst with pure ZrO_2 (Figure 10a). It should be noted that pure ZrO_2 also showed slight activity for CO_2 hydrogenation. For pure ZrO_2, formate species appeared at 10-20 cm^{-1} lower wavenumber than $CoZrO_x$ (10) catalyst. The adsorbed bidentate formate species is most stable when bonded to two Zr atoms.[29,54,58] The shifting of the peaks towards higher wavenumber on the $CoZrO_x$ (10) catalyst surface indicates a different bonding of formate species on the surface in comparison to pure ZrO_2. This could be a result of bonding of one O of formate with Co^{2+} instead of Zr^{4+} atom, indicating an adsorption site like Co-O-Zr (Figure 10a). Similar shifting of formate peak towards higher wavenumber was reported when formate was stabilized on interfacial site of In_2O_3/ZrO_2 catalysts, in which In and Zr are involved at the active site for the stabilization of formate species.[59]

In an experiment involving the decomposition of pre-adsorbed formic acid over ZrO_2 and $CoZrO_x$ (10) under He, CO was the primary product observed in mass spectrometer (Figure 10b). A single decomposition peak over ZrO_2 was centered at 350 °C, whereas two peaks were observed over $CoZrO_x$ (10) at 325 °C and 350 °C. The lower temperature peak, shown in red, was assigned to formate decomposition over Co-O-Zr interface site and the higher temperature peak, shown in blue,

represents decomposition over Zr-O-Zr surface. Therefore, we conclude that the formate species formed on and bound to Co-O-Zr sites decomposed selectively to CO just above 300 °C, resulting in high CO selectivity under all reaction conditions.

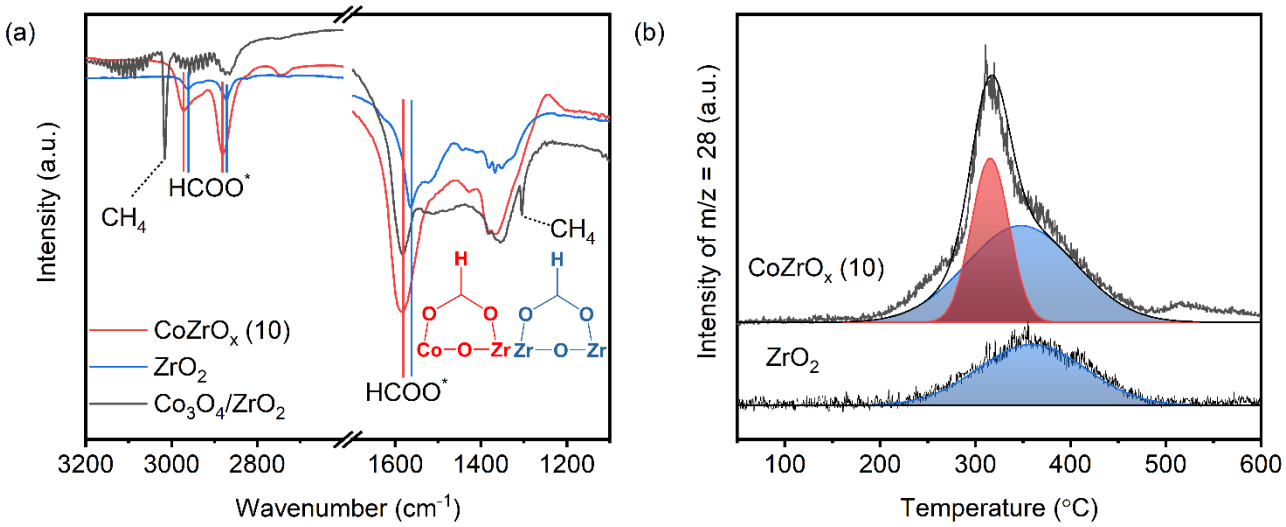

Figure 10: (a) Comparison of peak positions of formate species over $CoZrO_x$ (10), ZrO_2 and Co_3O_4/ZrO_2 during *in situ* DRIFTS study. Reaction condition: 340 °C, 0.1 MPa, H_2:CO_2 = 4:1. (b) Temperature programmed decomposition of pre-adsorbed formic acid decomposition over ZrO_2 and $CoZrO_x$ (10). Red and blue regions showed the fitting for $CoZrO_x$ (10).

In situ DRIFTS analysis over impregnated Co_3O_4/ZrO_2 also showed formation of formate species (Figure 10a). The peak positions of formate species over Co_3O_4/ZrO_2 were similar to that of $CoZrO_x$ (10). Formate species were not observed when Co_3O_4 was supported over silica (Figure S15). Therefore, we believe that even in impregnated catalyst the interface of Co and Zr is able to form formate species. However, the selectivity of CO over Co_3O_4/ZrO_2 was low due to methane formation. This was caused by further hydrogenation of CO species over Co metal particles and gaseous CH_4 was clearly observed in the IR spectra. This was supported CO hydrogenation activity over the

Co_3O_4/ZrO_2 catalyst under similar reaction condition (Figure S16), which produced CH_4 with 99 % selectivity.

Subsequent hydrogenation of gaseous CO to methane was not favored over doped catalyst as was the case of Co_3O_4/ZrO_2. CO adsorption was not observed at room temperature over doped catalyst whereas linear and bridged CO species were observed over impregnated catalyst in the DRIFTS spectrum (Figure 3b). The adsorption of CO molecule was also investigated using DFT. The optimized geometries of CO adsorption are shown in Figure 11. Adsorption energies for CO on pure ZrO_2, Co-ZrO_2, Co-ZrO_2_vo1 and Co-ZrO_2_vo2 were calculated to be -0.62, -0.93, -0.53 and -0.82 eV, respectively. CO molecule could bind either with the Co or Zr atoms but Co sites were energetically favored for CO adsorption on Co-ZrO_2 surfaces. Over Co-ZrO_2 surfaces without vacancy, CO adsorption was more favorable in comparison to CO_2 adsorption in carbonate mode shown in Figure 6b. However, on surfaces with oxygen vacancy, CO_2 adsorption was strongly favored in carbonate mode. Therefore, CO_2 would replace the CO molecule and make way for the next catalytic cycle. Exposing the $CoZrO_x$ (10) catalyst to CO and H_2 under the experimental reaction condition produced CH_4 as the major product confirming that presence of CO_2 inhibits further reaction of CO (Figure S16). Therefore, oxygen vacancies also helped in preventing strong adsorption of CO over Co atoms in presence of CO_2.

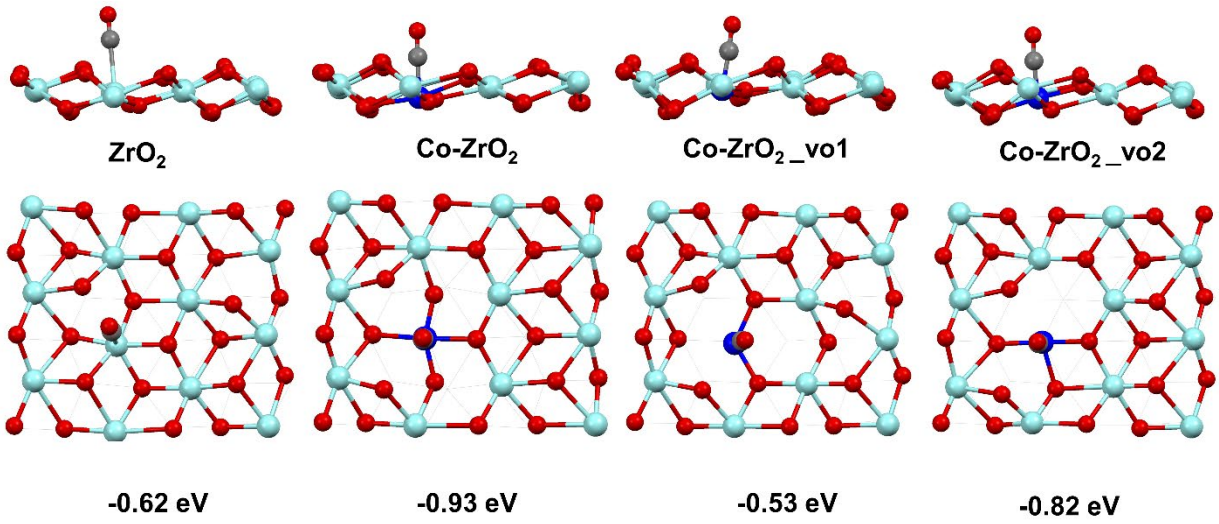

Figure 11: The most stable geometries for CO adsorption on ZrO_2, and Co-ZrO_2 surfaces. The atoms at top layer and the second layer were represented by ball and stick, respectively. The other atoms were omitted for clarity. The corresponding adsorption energies for CO molecule is shown at the bottom of each geometry. The Zr, O, Co and C atoms were represented in cyan, red, blue and gray colors, respectively.

Based on these observations, we propose the following mechanism for CO_2 hydrogenation over the surface of Co doped ZrO_2 catalyst (Figure 12). Owing to doping of Co^{2+} in ZrO_2, oxygen vacancies are formed because of charge imbalance in the crystal lattice. The vacancy promotes adsorption of CO_2 as carbonate species. H_2 dissociation happens over Co site followed by transfer of H to C atom of CO_2 to form a formate intermediate over the interfacial site of Co and Zr. Formate selectively decomposes to CO followed by removal of H_2O molecule without undergoing further hydrogenation to selectively yield CO.

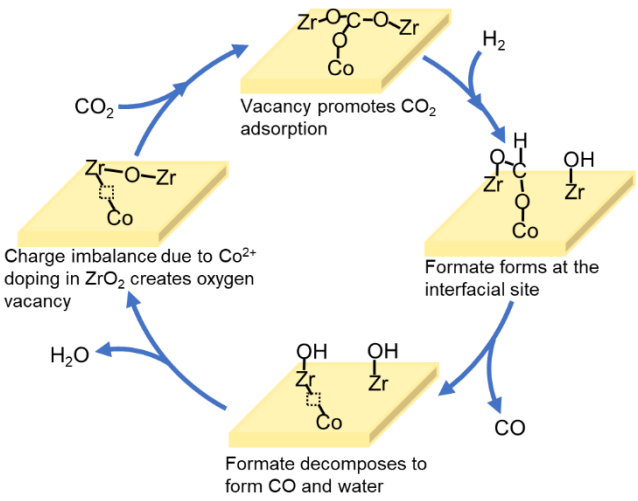

Figure 12: Schematic representation of reaction mechanism of CO formation from CO_2 over the Co doped ZrO_2 surface.

Conclusion

We showed that cobalt doped ZrO_2, prepared by co-precipitation method, is a highly active and selective catalyst for hydrogenation of CO_2 to CO. Co atoms were homogeneously distributed in tetragonal ZrO_2 matrix and maintained a Co^{2+} oxidation state. The charge imbalance between Co^{2+} and Zr^{4+} created oxygen vacancies and promoted chemisorption of CO_2. The doped catalyst produced CO with more than 95% selectivity and the activity was independent of change in reaction pressure, space velocity and H_2 to CO_2 ratio. In-situ and *operando* DRIFTS analysis showed that CO_2 was first hydrogenated to formate which could either hydrogenate further to methanol or decompose to CO. The atomically dispersed Co site in collaboration with neighboring Zr atom favored decomposition of formate to CO at temperatures above 300 °C. Atomic dispersion of Co also hampered the hydrogenation of CO to methane under the reaction conditions. DFT calculations confirmed that Co

doping in ZrO_2 leads to the formation of oxygen vacancies, which are necessary for CO_2 adsorption and formate formation. This study shows the importance of controlling the atomic interface between single atom and oxide supports to maximize the selectivity of a single product CO from CO_2 hydrogenation and can help in development of catalysts for C1 chemistry.

Author information

Corresponding Authors

Abhijit Shrotri - *Institute for Catalysis, Hokkaido University, Kita 21 Nishi 10, Kita-ku, Sapporo, Hokkaido 001-0021, Japan; email:* ashrotri@cat.hokudai.ac.jp

Atsushi Fukuoka - *Institute for Catalysis, Hokkaido University, Kita 21 Nishi 10, Kita-ku, Sapporo, Hokkaido 001-0021, Japan; email:* fukuoka@cat.hokudai.ac.jp

Authors

Nazmul Hasan MD. Dostagir - *Institute for Catalysis, Hokkaido University, Kita 21 Nishi 10, Kita-ku, Sapporo, Hokkaido 001-0021, Japan. Graduate School of Chemical Sciences and Engineering, Hokkaido University, Kita 13 Nishi 8, Kita-ku, Sapporo, Hokkaido 060-8628, Japan.*

Rattanawalee Rattanawan - *Institute for Catalysis, Hokkaido University, Kita 21 Nishi 10, Kita-ku, Sapporo, Hokkaido 001-0021, Japan.*

Min Gao - *Institute for Catalysis, Hokkaido University, Kita 21 Nishi 10, Kita-ku, Sapporo, Hokkaido 001-0021, Japan.*

Jin Ota - Institute for Catalysis, Hokkaido University, Kita 21 Nishi 10, Kita-ku, Sapporo, Hokkaido 001-0021, Japan. Division of Quantum Science and Engineering, Graduate School of Engineering, Hokkaido University, Kita 21-Nishi 10, Kita-ku, Sapporo, Hokkaido 001-0021, Japan

Jun-ya Hasegawa - *Institute for Catalysis, Hokkaido University, Kita 21 Nishi 10, Kita-ku, Sapporo, Hokkaido 001-0021, Japan.*

Kiyotaka Asakura - *Institute for Catalysis, Hokkaido University, Kita 21 Nishi 10, Kita-ku, Sapporo, Hokkaido 001-0021, Japan. Division of Quantum Science and Engineering, Graduate School of Engineering, Hokkaido University, Kita 21-Nishi 10, Kita-ku, Sapporo, Hokkaido 001-0021, Japan*

Notes

The authors declare no competing financial interest.

Supporting Information:

Details for catalyst preparation, characterization, and testing. DFT calculation parameters. N_2 adsorption isotherms, Lattice parameter change with doping, Zr and Co EXAFS, STEM-EELS analysis, long term reaction and characterization of used catalyst, schematic of DRIFT setup, additional experimental data, IR assignment, table showing comparison of catalytic activity with literature.

Acknowledgement

Part of this work was funded by the Integrated Materials Creation Chemistry Research Promotion Organization, Japan. XAFS analysis was performed under the approval of the Photon Factory Program Advisory Committee (Proposal No. 2019P018 and 2021G136). Support from Nanotechnology Platform Program of the Ministry of Education, Culture, Sports, Science and Technology (MEXT) is acknowledged. The authors acknowledge the help of Dr. Melbert Jeem and Ms. Naomi Hirai for STEM and EELS analysis. Assistance form Prof. Hiroshi Hirata for EPR analysis is also acknowledged. The theoretical work was financially supported by JSPS KAKENHI (20K05217, 20H02685), the Photo-excitonix Project at Hokkaido University and the MEXT project "Integrating Research Consortium on Chemical Science". Some of the computations were performed at Research Center for Computational Science (RCCS, Okazaki, Japan).

References

(1) Bao, J.; Yang, G.; Yoneyama, Y.; Tsubaki, N. Significant Advances in C1 Catalysis: Highly Efficient Catalysts and Catalytic Reactions. *ACS Catal.* **2019**, *9*, 3026–3053.

(2) Li, Y.; Gao, W.; Peng, M.; Zhang, J.; Sun, J.; Xu, Y.; Hong, S.; Liu, X.; Liu, X.; Wei, M.; Zhang, B.; Ma, D. Interfacial Fe_5C_2-Cu Catalysts toward Low-Pressure Syngas Conversion to Long-Chain Alcohols. *Nat. Commun.* **2020**, *11* , 1–8.

(3) Li, W. Z.; Liu, J. X.; Gu, J.; Zhou, W.; Yao, S. Y.; Si, R.; Guo, Y.; Su, H. Y.; Yan, C. H.; Li, W. X.; Zhang, Y. W.; Ma, D. Chemical Insights into the Design and Development of Face-Centered Cubic Ruthenium Catalysts for Fischer-Tropsch Synthesis. *J. Am. Chem. Soc.* **2017**, *139*, 2267–2276.

(4) Qi, J.; Finzel, J.; Robatjazi, H.; Xu, M.; Hoffman, A. S.; Bare, S. R.; Pan, X.; Christopher, P. Selective Methanol Carbonylation to Acetic Acid on Heterogeneous Atomically Dispersed ReO_4/SiO_2 Catalysts. *J. Am. Chem. Soc.* **2020**, *142*, 14178–14189.

(5) Lyu, S.; Wang, L.; Li, Z.; Yin, S.; Chen, J.; Zhang, Y.; Li, J.; Wang, Y. Stabilization of ε-Iron Carbide as High-Temperature Catalyst under Realistic Fischer–Tropsch Synthesis Conditions. *Nat. Commun.* **2020**, *11*, 1–8.

(6) Li, J.; He, Y.; Tan, L.; Zhang, P.; Peng, X.; Oruganti, A.; Yang, G.; Abe, H.; Wang, Y.; Tsubaki, N. Integrated Tuneable Synthesis of Liquid Fuels via Fischer–Tropsch Technology. *Nat. Catal.* **2018**, *1*, 787–793.

(7) Munnik, P.; De Jongh, P. E.; De Jong, K. P. Control and Impact of the Nanoscale Distribution of Supported Cobalt Particles Used in Fischer-Tropsch Catalysis. *J. Am. Chem. Soc.* **2014**, *136*, 7333–7340.

(8) Wang, W.; Wang, S.; Ma, X.; Gong, J. Recent Advances in Catalytic Hydrogenation of Carbon Dioxide. *Chem. Soc. Rev.* **2011**, *40*, 3703–3727.

(9) De, S.; Dokania, A.; Ramirez, A.; Gascon, J. Advances in the Design of Heterogeneous Catalysts and Thermocatalytic Processes for CO_2 Utilization. *ACS Catal.* **2020**, *10*, 14147–14185.

(10) Jangam, A.; Das, S.; Dewangan, N.; Hongmanorom, P.; Hui, W. M.; Kawi, S. Conversion of CO_2 to C1 Chemicals: Catalyst Design, Kinetics and Mechanism Aspects of the Reactions. *Catal. Today* **2020**, *358*, 3–29.

(11) Iablokov, V.; Beaumont, S. K.; Alayoglu, S.; Pushkarev, V. V.; Specht, C.; Gao, J.; Alivisatos, A. P.; Kruse, N.; Somorjai, G. A. Size-Controlled Model Co Nanoparticle Catalysts for CO_2 Hydrogenation: Synthesis, Characterization, and Catalytic Reactions. *Nano Lett.* **2012**, *12*, 3091–3096.

(12) Kwak, J. H.; Kovarik, L.; Szanyi, J. CO_2 Reduction on Supported Ru/Al_2O_3 Catalysts: Cluster Size Dependence of Product Selectivity. *ACS Catal.* **2013**, *3*, 2449–2455.

(13) Kwak, J. H.; Kovarik, L.; Szanyi, J. Heterogeneous Catalysis on Atomically Dispersed Supported Metals: CO_2 Reduction on Multifunctional Pd Catalysts. *ACS Catal.* **2013**, *3*, 2094–2100.

(14) Wu, H. C.; Chang, Y. C.; Wu, J. H.; Lin, J. H.; Lin, I. K.; Chen, C. S. Methanation of CO_2 and Reverse Water Gas Shift Reactions on Ni/SiO_2 Catalysts: The Influence of Particle Size on Selectivity and Reaction Pathway. *Catal. Sci. Technol.* **2015**, *5*, 4154–4163.

(15) Matsubu, J. C.; Yang, V. N.; Christopher, P. Isolated Metal Active Site Concentration and Stability Control Catalytic CO_2 Reduction Selectivity. *J. Am. Chem. Soc.* **2015**, *137*, 3076–3084.

(16) Su, X.; Yang, X. F.; Huang, Y.; Liu, B.; Zhang, T. Single-Atom Catalysis toward Efficient CO_2 Conversion to CO and Formate Products. *Acc. Chem. Res.* **2019**, *52*, 656–664.

(17) Zhu, J.; Zhang, G.; Li, W.; Zhang, X.; Ding, F.; Song, C.; Guo, X. Deconvolution of the Particle Size Effect on CO_2 Hydrogenation over Iron-Based Catalysts. *ACS Catal.* **2020**, *15*, 57.

(18) Wang, Y.; Winter, L. R.; Chen, J. G.; Yan, B. CO_2 hydrogenation over Heterogeneous Catalysts at Atmospheric Pressure: From Electronic Properties to Product Selectivity. *Green Chem.* **2021**, *23*, 249–267.

(19) Wang, A.; Li, J.; Zhang, T. Heterogeneous Single-Atom Catalysis. *Nat. Rev. Chem*. **2018**, *2*, 65–81.

(20) Millet, M. M.; Algara-Siller, G.; Wrabetz, S.; Mazheika, A.; Girgsdies, F.; Teschner, D.; Seitz, F.; Tarasov, A.; Levchenko, S. V; Schlögl, R.; Frei, E. Ni Single Atom Catalysts for CO_2 Activation. *J. Am. Chem. Soc.* **2019**, *141*, 2451–2461.

(21) Guo, Y.; Mei, S.; Yuan, K.; Wang, D. J.; Liu, H. C.; Yan, C. H.; Zhang, Y. W. Low-Temperature CO_2 Methanation over CeO_2-Supported Ru Single Atoms, Nanoclusters, and Nanoparticles Competitively Tuned by Strong Metal-Support Interactions and H-Spillover Effect. *ACS Catal.* **2018**, *8*, 6203–6215.

(22) Zhu, Y.; Yuk, S. F.; Zheng, J.; Nguyen, M.-T.; Lee, M.-S.; Szanyi, J.; Kovarik, L.; Zhu, Z.; Balasubramanian, M.; Glezakou, V.-A.; Fulton, J. L.; Lercher, J. A.; Rousseau, R.; Gutiérrez, O. Y. Environment of Metal−O−Fe Bonds Enabling High Activity in CO_2 Reduction on Single Metal Atoms and on Supported Nanoparticles. *J. Am. Chem. Soc.* **2021***, 143,* 5540-5549.

(23) Parastaev, A.; Muravev, V.; Huertas Osta, E.; van Hoof, A. J. F.; Kimpel, T. F.; Kosinov, N.; Hensen, E. J. M. Boosting CO_2 Hydrogenation via Size-Dependent Metal–Support Interactions in Cobalt/Ceria-Based Catalysts. *Nat. Catal.* **2020**, *3*, 526–533.

(24) Du, Y. P.; Bahmanpour, A. M.; Milošević, L.; Héroguel, F.; Mensi, M. D.; Kröcher, O.;

Luterbacher, J. S. Engineering the ZrO_2-Pd Interface for Selective CO_2 Hydrogenation by Overcoating an Atomically Dispersed Pd Precatalyst. *ACS Catal.* **2020**, *10*, 12058–12070.

(25) Kattel, S.; Liu, P.; Chen, J. G. Tuning Selectivity of CO_2 Hydrogenation Reactions at the Metal/Oxide Interface. *J. Am. Chem. Soc*. **2017**, *139*, 9739–9754.

(26) Ye, J.; Liu, C.; Mei, D.; Ge, Q. Active Oxygen Vacancy Site for Methanol Synthesis from CO_2 Hydrogenation on In_2O_3 (110): A DFT Study. *ACS Catal.* **2013**, *3*, 1296–1306.

(27) Wang, J.; Tang, C.; Li, G.; Han, Z.; Li, Z.; Liu, H.; Cheng, F.; Li, C. High Performance M_aZrO_x (Ma = Cd, Ga) Solid Solution Catalysts for CO_2 Hydrogenation to Methanol. *ACS Catal.* **2019**, *9*, 10253–10259.

(28) Wang, Y.; Chen, Z.; Han, P.; Du, Y.; Gu, Z.; Xu, X.; Zheng, G. Single-Atomic Cu with Multiple Oxygen Vacancies on Ceria for Electrocatalytic CO_2 Reduction to CH_4. *ACS Catal.* **2018**, *8*, 7113–7119.

(29) Wang, J.; Li, G.; Li, Z.; Tang, C.; Feng, Z.; An, H.; Liu, H.; Liu, T.; Li, C. A Highly Selective and Stable ZnO-ZrO_2 Solid Solution Catalyst for CO_2 Hydrogenation to Methanol. *Sci. Adv.* **2017**, *3*, 1–11.

(30) Dostagir, N. H. M.; Thompson, C.; Kobayashi, H.; Karim, A. M.; Fukuoka, A.; Shrotri, A. Rh Promoted In_2O_3 as a Highly Active Catalyst for CO_2 hydrogenation to Methanol. *Catal. Sci. Technol.* **2020**, *10*, 8196–8202.

(31) Shannon, R. D. Revised Effective Ionic Radii and Systematic Studies of Interatomic Distances in Halides and Chalcogenides. *Acta Crystallogr. Sect. A* **1976**, *32*, 751–767.

(32) Zhao, H.; Lu, H. Effect of Preparation Methods on Co/ZrO_2 Catalysts in Fischer-Tropsch Synthesis. *React. Kinet. Catal. Lett.* **2009**, *97*, 289–293.

(33) Chen, J. G.; Sun, Y. H. The Structure and Reactivity of Coprecipitated $Co\text{-}ZrO_2$ Catalysts for Fischer-Tropsch Synthesis. *Stud. Surf. Sci. Catal.* **2004**, *147*, 277–282.

(34) Li, W.; Liu, Y.; Mu, M.; Ding, F.; Liu, Z.; Guo, X.; Song, C. Organic Acid-Assisted Preparation of Highly Dispersed Co/ZrO_2 Catalysts with Superior Activity for CO_2 Methanation. *Appl. Catal. B Environ.* **2019**, *254*, 531–540.

(35) Song, D.; Li, J.; Cai, Q. In Situ Diffuse Reflectance FTIR Study of CO Adsorbed on a Cobalt Catalyst Supported by Silica with Different Pore Sizes. *J. Phys. Chem. C* **2007**, *111*, 18970–18979.

(36) Kumar, N.; Jothimurugesan, K.; Stanley, G. G.; Schwartz, V.; Spivey, J. J. In Situ FT-IR Study on the Effect of Cobalt Precursors on CO Adsorption Behavior. *J. Phys. Chem. C* **2011**, *115*, 990–998.

(37) Scalbert, J.; Clémençon, I.; Lecour, P.; Braconnier, L.; Diehl, F.; Legens, C. Simultaneous Investigation of the Structure and Surface of a Co/Alumina Catalyst during Fischer-Tropsch Synthesis: Discrimination of Various Phenomena with Beneficial or Disadvantageous Impact on Activity. *Catal. Sci. Technol.* **2015**, *5*, 4193–4201.

(38) Singh, J. A.; Yang, N.; Liu, X.; Tsai, C.; Stone, K. H.; Johnson, B.; Koh, A. L.; Bent, S. F. Understanding the Active Sites of CO Hydrogenation on Pt-Co Catalysts Prepared Using Atomic Layer Deposition. *J. Phys. Chem. C* **2018**, *122*, 2184–2194.

(39) Khivantsev, K.; Biancardi, A.; Fathizadeh, M.; Almalki, F.; Grant, J. L.; Tien, H. N.; Shakouri, A.; Blom, D. A.; Makris, T. M.; Regalbuto, J. R.; Caricato, M.; Yu, M. Catalytic N−H Bond Activation and Breaking by a Well-Defined $Co^{II}_1O_4$ Site of a Heterogeneous Catalyst. *ChemCatChem* **2018**, *10*, 736–742.

(40) Lee, D.; Xia, Q. X.; Yun, J. M.; Kim, K. H. High-Performance Cobalt Carbonate Hydroxide Nano-Dot/$NiCo(CO_3)(OH)_2$ Electrode for Asymmetric Supercapacitors. *Appl. Surf. Sci.* **2018**, *433*, 16–26.

(41) Hadjiivanov, K.; Avreyska, V.; Tzvetkov, G.; Stefanov, P.; Chupin, C.; Mirodatos, C.; Marinova, T. S. Selective Catalytic Reduction of NO_x by Methane over Co/ZrO_2 Catalysts. *Surf. Interface Anal.* **2001**, *32*, 175–178.

(42) Jiang, S.; Zhang, R.; Liu, H.; Rao, Y.; Yu, Y.; Chen, S.; Yue, Q.; Zhang, Y.; Kang, Y. Promoting Formation of Oxygen Vacancies in Two-Dimensional Cobalt-Doped Ceria Nanosheets for Efficient Hydrogen Evolution. *J. Am. Chem. Soc.* **2020**, *142*, 18.

(43) Liu, Y.; Xia, C.; Wang, Q.; Zhang, L; Huang, A.; Ke, M; Song, Z. Direct Dehydrogenation of Isobutene over Zn-doped ZrO_2 Metal Oxide Hetergoneous Catalysts. *Catal. Sci. Technol.* **2018**, *8*, 4916-4924.

(44) Silva-Calpa, L. D. R.; Zonetti, P. C.; Rodrigues, C. P.; Alves, O. C.; Appel, L. G.; Avilleg, R. R. D. The $Zn_XZr_{1-X}O_{2-y}$ solid solution on m-ZrO_2: Creating O vacancies and improving the m-ZrO_2 redox properties. *J. Mol. Catal. A: Chem.* **2016**, *425*, 166-173.

(45) Pan, Y.-X.; Liu, C.-J.; Mei, D.; Ge, Q. Effects of Hydration and Oxygen Vacancy on CO_2

Adsorption and Activation on β-Ga_2O_3 (100). *Langmuir* **2010**, *26*, 5551–5558.

(46) Indrakanti, V. P.; Kubicki, J. D.; Schobert, H. H. Photoinduced Activation of CO_2 on TiO_2 Surfaces: Quantum Chemical Modeling of CO_2 Adsorption on Oxygen Vacancies. *Fuel Process. Technol.* **2011**, *92*, 805–811.

(47) Xia, W.; Wang, F.; Wang, L.; Wang, J.; Chen, K. Highly Selective Lanthanum-Modified Zirconia Catalyst for the Conversion of Ethanol to Propylene: A Combined Experimental and Simulation Study. *Catal. Letters* **2020**, *150*, 150–158.

(48) Chen, H. Y. T.; Tosoni, S.; Pacchioni, G. Adsorption of Ruthenium Atoms and Clusters on Anatase TiO_2 and Tetragonal ZrO_2 (101) Surfaces: A Comparative DFT Study. *J. Phys. Chem. C* **2015**, *119*, 10856–10868.

(49) Chen, H. Y. T.; Tosoni, S.; Pacchioni, G. A DFT Study of the Acid–Base Properties of Anatase TiO_2 and Tetragonal ZrO_2 by Adsorption of CO and CO_2 Probe Molecules. *Surf. Sci.* **2016**, *652*, 163–171.

(50) Sahki, R.; Benlounes, O.; Chérifi, O.; Thouvenot, R.; Bettahar, M. M.; Hocine, S. Effect of Pressure on the Mechanisms of the CO_2/H_2 Reaction on a Co-Precipitated $CuO/ZnO/Al_2O_3$ Catalyst. *React. Kinet. Mech. Catal.* **2011**, *103*, 391–403.

(51) Iloy; Jalama. Effect of Operating Temperature, Pressure and Potassium Loading on the Performance of Silica-Supported Cobalt Catalyst in CO_2 Hydrogenation to Hydrocarbon Fuel. *Catalysts* **2019**, *9*, 807.

(52) Schild, C.; Wokaun, A.; Baiker, A. On the Mechanism of CO and CO_2 Hydrogenation

Reactions on Zirconia-Supported Catalysts: A Diffuse Reflectance FTIR Study. Part II. Surface Species on Copper/Zirconia Catalysts: Implications for Methanol Synthesis Selectivity. *J. Mol. Catal.* **1990**, *63*, 243–254.

(53) Fisher, I. A.; Bell, A. T. In-Situ Infrared Study of Methanol Synthesis from H_2 / CO_2. *J. Catal.* **1997**, *172*, 222–237.

(54) Pokrovski, K.; Jung, K. T.; Bell, A. T. Investigation of CO and CO_2 Adsorption on Tetragonal and Monoclinic Zirconia. *Langmuir* **2001**, *17*, 4297–4303.

(55) Köck, E. M.; Kogler, M.; Bielz, T.; Klötzer, B.; Penner, S. In Situ FT-IR Spectroscopic Study of CO_2 and CO Adsorption on Y_2O_3, ZrO_2, and Yttria-Stabilized ZrO_2. *J. Phys. Chem. C* **2013**, *117*, 17666–17673.

(56) Dobson, K. D.; McQuillan, A. J. An Infrared Spectroscopic Study of Carbonate Adsorption to Zirconium Dioxide Sol-Gel Films from Aqueous Solutions. *Langmuir* **1997**, *13*, 3392–3396.

(57) Kattel, S.; Yan, B.; Yang, Y.; Chen, J. G.; Liu, P. Optimizing Binding Energies of Key Intermediates for CO_2 Hydrogenation to Methanol over Oxide-Supported Copper. *J. Am. Chem. Soc.* **2016**, *138*, 12440–12450.

(58) Korhonen, S. T.; Calatayud, M.; Outi I Krause, A. Structure and Stability of Formates and Carbonates on Monoclinic Zirconia: A Combined Study by Density Functional Theory and Infrared Spectroscopy. *J. Phys. Chem. C* **2008**, *112*, 16096–16102.

(59) Chen, T. Y.; Cao, C.; Chen, T. B.; Ding, X.; Huang, H.; Shen, L.; Cao, X.; Zhu, M.; Xu, J.; Gao, J.; Han, Y. F. Unraveling Highly Tunable Selectivity in CO_2 Hydrogenation over

Bimetallic In-Zr Oxide Catalysts. *ACS Catal.* **2019**, *9*, 8785–8797.

For Table of Contents Only